J. Am. Soc. Mass Spectrom. (2016) 27:699–708
DOI: 10.1007/s13361-016-1333-0

RESEARCH ARTICLE

Target Plate Material Influence on Fullerene-C_{60} Laser Desorption/Ionization Efficiency

Guido P. Zeegers, Barbara F. Günthardt, Renato Zenobi

Department of Chemistry and Applied Biosciences, ETH Zürich, Vladimir-Prelog-Weg 3, CH-8093, Zürich, Switzerland

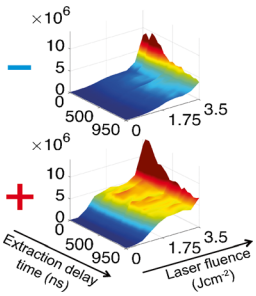

Abstract. Systematic laser desorption/ionization (LDI) experiments of fullerene-C_{60} on a wide range of target plate materials were conducted to gain insight into the initial ion formation in matrix-assisted laser desorption/ionization (MALDI) mass spectrometry. The positive and negative ion signal intensities of precursor, fragment, and cluster ions were monitored, varying both the laser fluence (0–3.53 Jcm^{-2}) and the ion extraction delay time (0–950 ns). The resulting species-specific ion signal intensities are an indication for the ionization mechanisms that contribute to LDI and the time frames in which they operate, providing insight in the (MA)LDI primary ionization. An increasing electrical resistivity of the target plate material increases the fullerene-C_{60} precursor and fragment anion signal intensity. Inconel 625 and Ti90/Al6/V4, both highly electrically resistive, provide the highest anion signal intensities, exceeding the cation signal intensity by a factor ~1.4 for the latter. We present a mechanism based on transient electrical field strength reduction to explain this trend. Fullerene-C_{60} cluster anion formation is negligible, which could be due to the high extraction potential. Cluster cations, however, are readily formed, although for high laser fluences, the preferred channel is formation of precursor and fragment cations. Ion signal intensity depends greatly on the choice of substrate material, and careful substrate selection could, therefore, allow for more sensitive (MA)LDI measurements.

Keywords: C_{60}, Electrical conductivity, Electrical resistivity, Electrospray deposition, Fullerene, Ionization mechanism, LDI, MALDI, Thermal conductivity

Received: 10 September 2015/Revised: 3 December 2015/Accepted: 30 December 2015/Published Online: 19 February 2016

Introduction

One of the main questions that remain to be solved for MALDI, a well-established soft-ionization analytical technique developed in the mid-1980s [1, 2], concerns the origin of the charge: how does the charge separation come about and how is it maintained? Does the charge originate from the matrix or the substrate? How is the ion yield limited by initial charge separation efficiency and/or the subsequent neutralization? Are only the analyte and matrix molecules involved in these processes or does the surface underneath also play a role and, if so, is it purely a thermal role or do electrical effects contribute?

Some consensus has been reached in the form of a two-step framework, where the first step comprises the initial charge separation, followed by the second charge transfer step, occurring during the MALDI plume development [3, 4]. For this initial charge separation, the following theories and models have been developed:

1. (Multi-) photon ionization [5]:

$$M \xrightarrow{(n)h\nu} (M)^{\bullet+} + e^- \quad (1)$$

where the photon absorption depends on the photoionization cross section. If the laser wavelength happens to be in resonance with an excited state of the molecule, absorption of a second photon then ionizes the molecule, via 1 + 1 resonance enhanced multiphoton ionization (REMPI) [6].

2. (Photo-) thermal ionization [7, 8]:

$$M \xrightarrow{((n)h\nu/\Delta)} (M)^{\bullet+} + e^- \quad (2)$$

where, following photo-excitation, thermionic emission by vibronic coupling is proposed as the primary ionization route.

Electronic supplementary material The online version of this article (doi:10.1007/s13361-016-1333-0) contains supplementary material, which is available to authorized users.

Correspondence to: Renato Zenobi; *e-mail:* zenobi@org.chem.ethz.ch

3. Energy pooling [9, 10]:

$$M + M \overset{(n)hv}{\rightarrow} M^* + M^{*\,\Delta,} \overset{pooling}{\rightarrow} M + (M)^{\bullet +} + e^- \quad (3)$$

4. Charge (electron or proton) disproportionation [11] ionization (e.g., pseudo proton transfer due to energy transfer induced disproportionation [12], or excited state proton transfer [13]), leading to equal amounts of oppositely charged ions.
5. Cluster-based 'lucky survivor' model [14, 15], where preformed ions are liberated and unevenly divided over clusters, giving them a charge. Clusters decompose and ions that are not neutralized can be detected.
6. Polar fluid model [16], where a vaporizing matrix forms a dense polar fluid, which enables ion pair separation.
7. Substrate photoelectron production [17], where an electron is liberated from the substrate by a photon exceeding the substrate's work function (φ):

$$[Metal] \overset{(n)hv}{\rightarrow} [Metal]^{\bullet +} + e^- \quad (4)$$

$$K_{max} = hf - \varphi \quad (5)$$

This electron has a maximum kinetic energy (K_{max}) of the photon energy (hf) minus the substrate's work function (φ); φ depends on the substrate material's surface structure and is, therefore, influenced directly by localized temperature changes, surface defects, and sample coverage [18], which make it a difficult parameter to assess for (MA)LDI experiments.

While the ionization energy (IE) determines how much energy is required to separate an electron from a neutral species to become a cation, the electron affinity (χ) plays the key role in anion formation, determining the amount of energy required or released upon ionization:

$$M + e^- \rightarrow (M)^{\bullet -} \quad (6)$$

Our work focuses on the initial charge generation step and systematically investigates the charge separation efficiency in relation to the target plate material's conductive properties by stepwise varying both the laser fluence and the extraction delay time for positive and negative polarity.

The extraction delay time was originally developed to gain a higher resolution [19, 20] since it compensates for the kinetic energy distribution among the species present in the MALDI plume, generated by the laser pulse. Here, however, the extraction delay was employed to extract all ion species present in the plume after a certain time to verify their presence during the various plume development stages. As long as neutralization rates are sufficiently low, any delayed ionization processes within the investigated time interval should thus become apparent.

Important for the outcome of a (MA)LDI experiment are the chosen laser parameters (here: nitrogen laser; λ = 337 nm; photon energy: 3.67 eV) and the fluence applied. The laser fluence determines whether and how much material is desorbed or ablated (surface versus volume models) [21]. To take this effect into account, the laser fluence was varied in a stepwise fashion from 0 to the maximum operating fluence (3.53 Jcm^{-2}) for each extraction delay time used.

Although LDI cannot be fully compared with MALDI because of the absence of a matrix, it can provide some insight into the initial step, where the matrix absorbs the laser light and becomes charged. To enable easy integration of the acquired spectra, necessary for determining ion signal intensities for each substrate material tested, fullerene-C_{60} was chosen as a model.

Besides having been studied as analytes with MALDI-MS, fullerenes have also been applied as MALDI matrices themselves, since their extended conjugated π–system enables them to absorb the incoming UV-photons. For the non-fluorescent fullerene-C_{60} the photon energy would then be converted into thermal energy via ultrafast non-radiative relaxation, resulting in the abrupt overheating of the matrix crystal [16, 22]. The easily identifiable fragmentation pattern, namely the sequential loss of C_2 units [23], and its ability to form clusters, make fullerene-C_{60} the ideal candidate for quantification. Additionally, the absence of protons reduces the number of primary ionization pathways. The IE has been calculated and experimentally found to be 7.6 eV [24–28], whereas χ is in the range of 2.6–2.8 eV [29–31]. Fullerene-C_{60} is thought to be able to store large amounts of energy through rapid conversion of electronic excitation to vibrational excitation because of its many degrees of freedom, thereby enabling delayed ionization processes [32]. Fullerene-C_{60} was also found to be an effective electron scavenger over a remarkably broad energy range up to ca. 14 eV [33], enabling anion formation.

Experimental

Materials

MALDI target plate inset materials were either purchased at Goodfellow Cambridge Ltd. (Huntingdon, United Kingdom): Ti90/Al6/V4, thickness 1.0 mm; Iron/Nickel, Fe52/Ni48, thickness 0.75 mm; Invar, Fe64/Ni36, thickness 1.0 mm; Cobalt/Chromium/Tungsten/Nickel/Iron/Manganese, Co50/Cr20/W15/Ni10/Fe3/Mn2, thickness 0.25 mm, Inconel 625, Ni61/Cr22/Mo9/Fe5, thickness 0.3 mm; vitreous carbon, thickness 1.0 mm; Waspaloy thickness 1.0 mm, or acquired from the ETH Zürich physics shop (copper, brass, phosphor bronze, anticorodal-110, peraluman-101, stainless steel 1.4301, each thickness 1.0 mm; beryllium copper, thickness 0.8 mm). Height differences were compensated with a copper support to ensure a total substrate inset height of 1.0 mm (±0.01 mm) to prevent artifacts arising from higher or lower extraction field

strengths. All insets were cut to a size of 50 × 50 mm. An overview of their respective average conductive properties is shown in Table 1, revealing the exponential decay of resistivity with increasing thermal conductivity.

Elsterglanz polish (Ahrenshof GmbH, Zwachau bei Leipzig, Germany) was used to clean the inset surfaces. Solvents used for the subsequent inset cleaning procedure, n-hexane (Chromasolv for HPLC; ≥95%) and methanol (LiChrosolv, Reag. Ph. Eur) were purchased from Merck KGaA, Darmstadt, Germany, and Sigma-Aldrich Chemie GmbH, Steinheim, Germany, respectively. Xylene (≥97.0%), used to dissolve fullerene-C_{60} for electrospray deposition, CsI, used for calibration, and fullerene-C_{60} (99.5%) were purchased from Sigma-Aldrich Chemie GmbH, Steinheim, Germany. Copper tape (6.0 mm wide, thickness 0.07 mm; Scotch 1181), used to secure the MALDI target plate insets, was purchased from 3 M GmbH, Rüschlikon, Switzerland. Before each new sample deposition, the insets were cleaned, which was done by using Elsterglanz as polishing agent to scrub the surface extensively. Subsequently, the insets were submerged in n-hexane and sonicated for 15 min, followed by a second 15 min sonication round in methanol. Insets were left to dry before being mounted in the deposition setup.

Sample Deposition

In order to ensure reproducible results [34], a custom-made spray deposition setup was built (see Supporting Information: Supplementary Figure S1A). A 0.250 µg/mL fullerene-C_{60} solution in xylene was prepared by 15 min sonication and was subsequently stored in a brown glass bottle to prevent contamination and decomposition [35]. This solution was pumped through an electrospray source (Waters AG, Dättwil, Switzerland; 3.5 kV; 5 bar pressurized air) at a 2.0 µL/min. flow rate by a Harvard apparatus syringe pump (type 22), resulting, after a 1 min spray time, in a deposition of max. 500 ng fullerene-C_{60} on a surface with roughly a 5 mm diameter, which was reduced to a ø 3 mm sample spot surface by means of Teflon masks. This and an automated Thorlabs 3D stage enabled the reproducible application of 100 spots in a 10 × 10 array for each substrate inset.

Table 1. Resistivity and Thermal Conductivity at Room Temperature of the Substrate Materials used as LDI Target Plate Insets

Material	Resistivity (µΩcm)	Thermal conductivity ($Wm^{-1}K^{-1}$)
Copper	1.69	401
Anticorodal-110	3.6	187
Peraluman-101	4.1	135
Brass	6.4	125
Beryllium copper	8.4	90
Phosphor bronze	13.5	63
Fe52/Ni48	49	16.7
Stainless steel 1.4301	72	16.2
Invar	80	13
Co50/Cr20/W15/Ni10/Fe3/Mn2	88.6	9.4
Waspaloy	125	10.7
Inconel 625	129	9.8
Ti90/Al6/V4	168	5.8
Glassy carbon	400	6.3

Values (taken from material property information provided by Goodfellow GmbH, Germany) are displayed as averages, since conductivity properties may vary from batch to batch. Note that the resistivity decays exponentially with increasing thermal conductivity

Mass Spectrometry

By milling a 102.2 × 51.2 × 1 mm structure out of commercial MALDI target plates, inserting two insets (ca. 50 × 50 mm), and securing them with conductive copper tape, several different substrate materials could be tested, as shown in Supplementary Figure S1B. The milled out structure was made a bit larger as required to compensate for irregularities in inset dimensions. The copper tape served a second purpose by covering the trenches in between insets and the MALDI target plate, thereby ensuring a proper electric field distribution.

Measurements were taken on an Autoflex I MALDI-Time-of-Flight (TOF) mass spectrometer (Bruker Daltonik, Bremen, Germany; Compass for flexSeries 1.3 software suite; nitrogen laser MNL 100, Lasertechnik Berlin: λ: 337 nm, typical pulse width: 3 ns FWHM) at a wavelength at which fullerene-C_{60} absorbs well [36]. The instrument allows for increasing the laser fluence as well as the extraction delay time gradually in a semi-automated fashion and for measuring in linear and reflectron mode as well as with either a positive or a negative polarity. All measurements reported here were recorded in the reflectron mode.

Experiments on the Autoflex were carried out with the flexControl software (ver. 3.3; build 108). The applied potential differences, depending on the polarity chosen, were ±20.00 kV on the MALDI target plate, ±17.30 kV on the extraction plate, ±8.50 kV on the lens, and ±20.00 kV on the reflector; the multichannel plate reflector detector was set at 1.40 kV. The laser power was varied from 0 to 3.52 Jcm^{-2} with 10% increments, and the extraction delay time was varied with 50 ns increments from 0 to 950 ns. Spectra were recorded over a *m/z* 100–2500 range in order to include most fullerene-C_{60} fragments, the C_{60}-molecular ion, and charged clusters composed of either two or three fullerene-C_{60} (fragment) ions. Since fullerene-C_{60} fragmentation occurs almost instantly upon increasing the laser fluence, the *m/z* 365–730 range was chosen in order to include all singly charged fragments of the precursor peak (*m/z* 720) and the precursor peak itself to calculate the ion signal intensity for inter-material comparison.

The MALDI target plate was positioned according to three milled out reference points. Each sample spot was measured in a 5 × 5 array (see Supplementary Figure S1B), where each array spot was 150 µm from the next spot in order to avoid overlap of the ø 55 µm laser beam spot. Each array spot was irradiated 10 times at a 50 Hz repetition rate to ensure that no fullerene-C_{60} was left for the highest applied laser fluence. The 250 resulting spectra were averaged by the flexControl software and exported to flexAnalysis.

Data Processing

The raw data were converted to .txt-files in flexAnalysis (ver. 3.3; build 80). These were subsequently processed by MATLAB-scripts, which integrated the spectra over the *m/z* regions of interest (*m/z* 365–730 and 1040–2170), and three of these experiments were averaged to yield a 3D-plot of both the ion signal intensity for these specific *m/z* ranges versus extraction delay time and laser fluence, as well as a standard deviation plot, where the standard deviation was expressed as the percentage of the mean value. The *m/z* 365–730 range comprises the fullerene-C_{60} precursor peak, as well as its fragments up to half the molecule's size, and the *m/z* 1040–2170 range was chosen to monitor the cluster ions formed, together enabling establishing which species are preferably formed for the chosen laser fluence and the extent of their neutralization during plume development. Owing to the tailing of the precursor peak at *m/z* 730 (caused by delayed ionization [37]), the lower limit of *m/z* 1040, just below 1.5× the molecular weight of fullerene-C_{60}, was chosen. The upper limit of *m/z* 2170 was chosen to be just above three times fullerene-C_{60}'s molecular weight.

Results

The resulting fullerene-C_{60} layers were analyzed by deposition on a microscopy cover slip. Light microscopy and subsequent surface profiling of this cover slip, Figure 1a and b, respectively, revealed the formation of fullerene-C_{60} nano-crystallites of several 100 nm in height with similar morphologies as previously reported [38].

To assess the impact of the laser shots on the crystallites via light microscopy, the experiment was carried out once on a glass microscopy slide, which was coated with indium tin oxide, as an optically transparent conductive layer, required for application of the ±20 kV potential. The effect of the laser pulses can be seen in Figure 1c. The laser partly destroys the (at 337 nm slightly absorbing [39]) indium tin oxide layer at the highest applied laser fluence (dark ellipsoid spot). Fullerene-C_{60} LDI experiments generally resulted in mass spectra as indicated in Figure 3d, which were used for relative ion signal intensity determination for the indicated *m/z* ranges. The spectral patterns did not show any significant *m/z* shifts when the extraction delay time was varied; only the resolution was somewhat affected.

For the highest four laser fluence values, destruction of the glassy carbon was observed. Care should also be taken when interpreting the results for the aluminum alloys for high laser fluence because the aluminum lit up upon laser irradiation, indicating that either the oxide layer was removed or that the surface started to melt. Since melting would also fundamentally change the material's work function [40], the data on aluminum alloys (anticorodal-110, peraluman-101, and Waspaloy), as well as glassy carbon, have been left out of the final analysis. Despite the observed substrate material destruction, no metal-fullerene-C_{60} adducts were observed: no mass shifts or metal cation-specific isotopic patterns could be identified. All substrate material-specific ion signal intensity data, including standard deviation plots, are given in Supplementary Figure S2 and Supplementary Figure S3, respectively.

As can be seen in Figure 2 and in Supplementary Figure S2, the precursor and fragment cation signal intensity increases with increasing laser fluence. A clear ionization fluence threshold was not observed since for the entire covered laser fluence range, fullerene-C_{60} ionization was observed. The steep signal intensity increases could be an indication for the transition from surface desorption to volume ablation. The same observations were made for the cluster cation species.

When the laser fluence is increased even further, the cluster cation signal intensity decreases or does not further increase, and an increase in precursor and fragment cations is observed. This was observed for all materials tested, as displayed in Supplementary Figures S2 and S4, where the ion signal intensities during the first 200 ns for two different laser fluence values, 1.96 and 3.53 Jcm^{-2}, were averaged for both the precursor and fragment, as well as the cluster ions. This time interval was chosen because the highest precursor and fragment ion signal intensities were always observed for extraction delay times between 0 and ca. 200 ns at the highest measured laser fluence (3.53 Jcm^{-2}). Comparing both laser fluence values, it becomes apparent that when the laser fluence is increased the precursor and fragment cation signal intensity increases at the cost of the cluster cation signal intensity, which does not increase proportionally, or even declines. Cluster anions are hardly, if at all, formed and the precursor and fragment anion signal intensity increases for increasing laser fluence as well.

The averaged data points for the highest laser fluence from Supplementary Figure S4 were also used for further analyzing the influence of the substrate's conductive properties, as displayed in Figure 3.

In Figure 3, a trend between electrical resistivity and anion signal intensity becomes apparent: precursor and fragment anion signal intensities increase monotonically with the substrate material resistivity. The same effect is observed comparing the thermal conductivity (not shown): when the thermal conductivity is reduced, the signal intensity increases exponentially, which can be attributed to the fact that electrical and thermal conductivity are related (see Table 1). The presence of cluster cations obscures any resistivity dependence for the precursor and fragment cations.

Discussion

Cluster Ion Formation and Stability

During LDI experiments, stable fullerene clusters, probably coalesced fullerene products, are formed [41], which through electron loss or attachment appear as cluster ions. Cationic coalesced fullerene products do not easily dissociate, as was shown for C_{118}^{+} through surface collision experiments with energies up to 200 eV [41]. Multiple collisions with xenon atoms at a translational energy of 800 eV do not induce their dissociation either [37]. The survival probability of the anionic

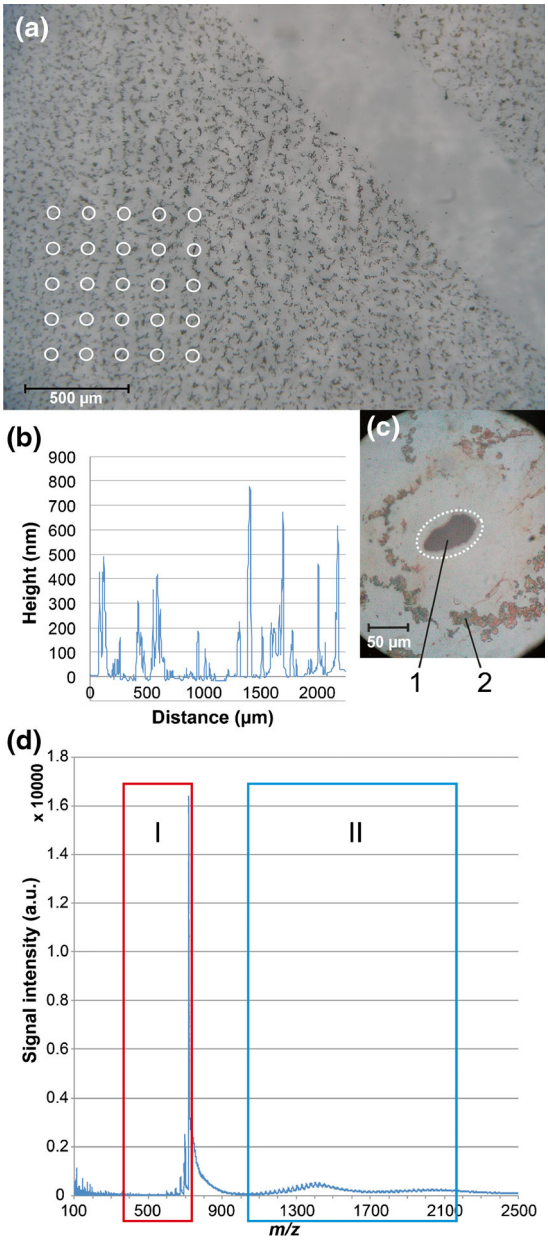

Figure 1. (**a**) Magnification of fullerene-C_{60} electrosprayed on a microscopy cover slip. Fullerene-C_{60} tends to aggregate into small crystallites on the glass slide. Similar patterns were observed for metal substrates. The white circles indicate the ablation array. (**b**) Surface profile of fullerene-C_{60} on a glass slide surface taken from left to right, recorded with a Tencor P-11 Surface Profiler. Fullerene-C_{60} crystallites are clearly discernable. (**c**) The destroyed indium tin oxide layer (1) and the remaining fullerene-C_{60} crystallites (2) after laser desorption/ionization. The irradiated area has been indicated with a white dotted line. (**d**) Typical fullerene-C_{60} mass spectrum in positive reflectron mode (*m/z* 100–2500), with the two analyzed regions 365–730 (I; red box) and *m/z* 1040–2170 (II; blue box), denoting the precursor and fragment cations and cluster cations, respectively. Ion signal integration for the specified *m/z* ranges for each applied laser fluence and extraction delay time, gave rise to substrate material-specific and polarity-dependent ion signal intensity plots, such as the interpolated heat maps shown in Figure 2 for Ti90/Al6/V4

clusters decreases with an increase in temperature [42], but increases for higher fullerene anions [33, 43, 44].

Ionization Reactions

Upon laser firing, the following ionization reaction could occur,

$$C_{60} \xrightarrow{((n)h\nu)/\Delta} C_{60}^{\bullet +} + e^{-} \tag{7}$$

the underlying principle being either multiphoton ionization [45] (requiring three 337 nm photons) or (photo-)thermal ionization to overcome the IE of 7.6 eV. This reaction equally applies to the coalesced products formed under the LDI conditions. Maximum photoabsorption cross-section values for fullerene-C_{60} of 0.12–0.14 nm^2 have been reported for photon energies between 20 and 25 eV [46]. The photoionization cross section for fullerene-C_{60} at a photon energy of 26 eV was reported to be close to 0.05 nm^2 [47]. When the photon energy exceeds a certain threshold (40.8 eV [28]; 47 eV [47]) the formation of fullerene-C_{60} fragment cations should be taken into account.

When reaction 7 occurs, an electron is generated, which can subsequently become attached to a fullerene-C_{60} molecule to form an anion:

$$C_{60} + e^{-} \xrightarrow{((n)h\nu)/\Delta} C_{60}^{\bullet -} \tag{8}$$

Besides electrons originating from cation production, those that might be liberated from the metal substrate could potentially add to the fullerene-C_{60} anion formation as well. The same electron attachment could, in principle, account for the formation of cluster anions.

In the region from 1 to 6 eV, the electron attachment cross section was reported to be 0.36 ± 0.03 nm^2 [48]. Much higher electron attachment cross sections were reported for lower energy electrons and higher molecular temperatures [42, 49]. It has been proposed that low energy electrons become temporarily bound in a region of attractive potential, surrounded by a repulsive potential barrier, a so-called shape resonance, followed by electronic-to-vibrational energy conversion or even photon emission leading to a more stable and relaxed anion configuration. Resonance structures at 0.2, 1.5, 4.5, 5.5, and 8 eV were attributed to electron attachment into higher fullerene-C_{60} electronic states [50]. Several research groups have reported on electron capture threshold values close to zero energy [44, 49, 51]. The outcome of ab initio calculations stress the importance of angular correlation in binding an excess electron, which makes fullerene-C_{60} special compared with molecular anions with a comparable electron affinity [52].

Looking at the aforementioned cross sections for photoionization, leading to cation formation, and for anion generating electron attachment, one would expect the

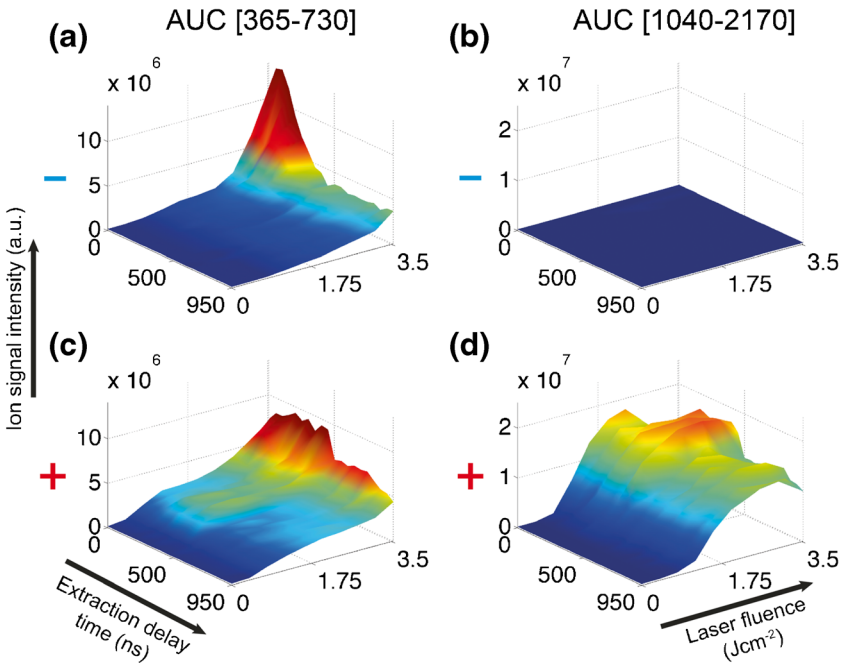

Figure 2. Positive and negative ion signal intensities (AUC: area under the curve) for fullerene-C_{60}, laser-desorbed from Ti90/Al6/V4 (ρ=168 μΩcm), for both mass ranges (*m/z* 365–730 and 1040–2170). The data, represented here as a heat map, are the interpolated data points acquired by varying the extraction delay time from 0 to 950 ns with 50 ns intervals and the laser fluence from 0 to 3.51 Jcm^{-2} with 10% increasing steps. Note the high precursor and fragment cation and anion signal intensities at the highest applied laser fluence and during the first 200 ns, most notably the sharp anion peak (**a**), which exceeds its cationic counterpart (**c**) by ca. 140%, as well as the complete absence of cluster anions (**b**). The cluster cation signal intensity (**d**) decreases and, simultaneously, the precursor and fragment cation increases (**c**) for the highest applied laser fluences. Cationic species seem to be stable for at least 1 μs, whereas anion precursor and fragment signal intensity decreases rapidly after 150 ns

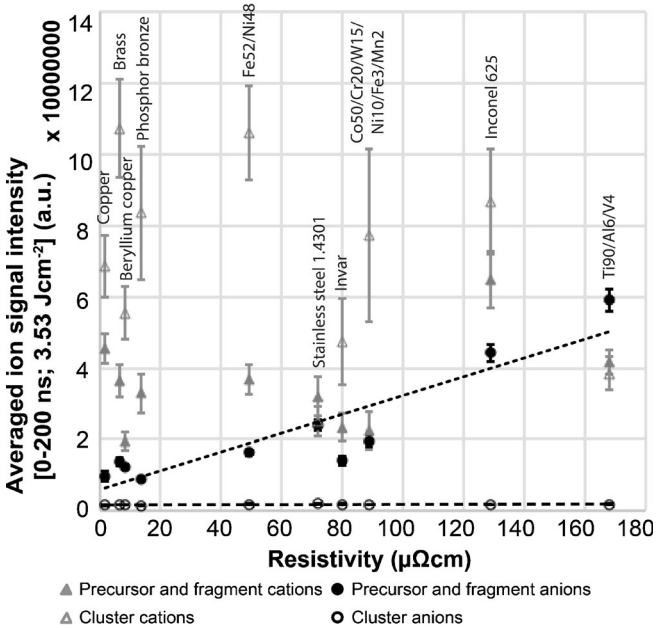

Figure 3. The averaged fullerene-C_{60} precursor and fragment [*m/z* 365–730] as well as the cluster ion [*m/z* 1040–2170] signal intensities recorded between 0 and 200 ns extraction delay time at a 3.53 Jcm^{-2} laser fluence versus the average reported target plate material electrical resistivity for both polarities. Cluster anions were hardly, if at all, formed, as indicated by the dashed line. The dotted line indicates the linear trend for precursor and fragment anion signal intensity for increasing substrate resistivity

number of anions to exceed those of the cations if electrons were plentiful and not generated via fullerene-C_{60} photoionization. Bimolecular reactions, such as anion formation by means of electron attachment, are statistically less likely to occur than unimolecular reactions, such as cation formation by electron detachment, and in this case the bimolecular anion formation is limited by the electron production via fullerene-C_{60} photoionization, unless additional electrons are liberated from the substrate's surface.

Neutralization Reactions

Following ionization, subsequent neutralization can occur. In case of cationic species (bimolecular) cation neutralization reactions, aided by Coulombic attraction, could reduce the cation signal intensities:

$$C_{60}^{\bullet +} + e^- \rightarrow C_{60} \quad (9)$$

$$\{C_{60}\}_n^{\bullet +} + e^- \rightarrow \{C_{60}\}_n \quad (10)$$

Anionic species, on the other hand, could get neutralized via (unimolecular) electron autodetachment (EAD) [53], occurring at 6.5 eV and above [51]:

$$C_{60}^{\bullet -} \rightarrow C_{60} + e^- \quad (11)$$

Finally, the neutralization of the formed ions could occur through the encounter of, and charge exchange between, two oppositely charged fullerene-C_{60} ions:

$$C_{60}^{\bullet+} + C_{60}^{\bullet-} \rightarrow C_{60} + C_{60} \quad (12)$$

Cluster Ions Versus Precursor and Fragment Ions

The data (Figure 2 and Supplementary Figure S2) underline the stability of the cationic species formed [41]. Cluster anions, although previously reported [54], were not observed at all, indicating that their formation is not as likely as that of their cationic counterparts, and might be dependent on the chosen experimental settings [51]. As can be deduced from Figure 2c, d, and Supplementary Figure S4, a laser fluence exceeding 1.96 Jcm^{-2} tends to diminish the increase or even decrease the cluster cation signal intensity, compared with the precursor and fragment cations. Multiphoton absorption and the resulting high internal excitation of fullerenes is known to lead to both fragmentation [28] and delayed ionization [45]. Rapid, increased fragmentation explains the observed simultaneous increase in the precursor and fragment cations rather than delayed cluster cation decomposition during plume development. Delayed ionization, due to EAD, explains the fullerene-C_{60} precursor peak tailing (Figure 2d), which can extend into the microsecond timeframe [37, 45]. The EAD formation of precursor, fragment, and cluster cations obscures any trends with the target plate material's conductive properties because they can be formed within a wider timeframe and are, therefore, not necessarily in the vicinity of the target plate upon formation.

Influence of the Substrate's Thermal Conductivity

The thermal conductivity, which is intrinsically linked to the electrical resistivity and work function through the material structure, determines the heat build-up rate at the irradiated substrate surface part: for a high thermal conductivity, the substrate is expected to heat up less and the ablated sample material amount to be lower, compared with a substrate with low thermal conductivity. Ideally, perhaps with a fully transparent and conductive target plate, only fullerene-C_{60} would be absorbing the laser light and not the target plate material. Since discrete crystallites are formed (Figure 1a), the target plate will always contribute to the absorption and local heat build-up and no clear separation can be made.

The ablated sample material amount depends on the laser pulse duration as well [55]. Shorter pulses of equal intensity should allow for less heat dissipation time, causing an increased localized heating. Depending on the laser used, the pulse duration can vary from the nanosecond-range, typically used for UV-MALDI (0.3–20 ns) [21, 56, 57], to picoseconds or even a few femtoseconds. A report comparing nanosecond and femtosecond laser data for fullerene-C_{60} found the formed anionic species to be similar, which was ascribed to thermalization in the ablation plasma [58].

The precursor and fragment anion and, to a lesser extent, the cation signal intensities were found to exponentially increase with a decreasing thermal conductivity in the very narrow range of the low thermally conductive materials, which is due to the relationship with electrical resistivity. Therefore, the trend was further analyzed with regards to the electrical resistivity, as shown in Figure 3.

Influence of the Substrate's Electrical Resistivity

When discussing the role of the substrate material's electrical resistivity, we should take into account the migration and neutralization of the oppositely charged species. For a positive polarity on the target plate, electrons and anionic species are attracted by the target plate and will be neutralized there, whereas cations will be propelled to the detector as soon as the ion extraction potential is applied. For a negative polarity on the target plate, cationic species will migrate towards the target plate as soon as ion extraction occurs and will be neutralized, whereas anions and electrons are accelerated towards the detector. The arising electron deficit or excess at the substrate surface, causing a transient reduction of the extraction potential, will have to be restored by a current from the power supply to the target plate in order to guarantee a homogenous ion-extracting electric field. Here the target plate material's resistivity comes into play.

These effects would explain this anion signal intensity increase for increasing electrical resistivity (Figure 3). The transiently reduced potential difference between the area of cation impact on the target plate and the extraction plate will affect the transport towards the detector of the anionic species and the electrons present in the plume. This will, therefore, allow more time for bimolecular reactions to occur between electrons and neutral molecules, promoting anion formation, and it will enhance cation neutralization, while electrons and cationic species are allowed more time to interact in the plume. This could explain the observations for Ti90/Al6/V4, where the anion signal intensity exceeded its cationic counterpart. The target plate resistivity determines how long it will take to counteract this local electric field perturbation. This theory is in line with the observation that for an increased extraction potential, the relative intensity of fullerene-C_{60}'s lower energy peak for electron attachment decreases [51], stressing the importance of the instrumental settings for anion formation.

Proposed Mechanisms

It is important to note that all the aforementioned ionization and neutralization reactions could occur independent of the measuring polarity. Taking into account the stability of the cluster ions, the possible coalescence, ionization, and neutralization reactions are summarized in Figure 4. The extent of cluster formation mainly depends on the applied laser fluence. Whether all anionic species

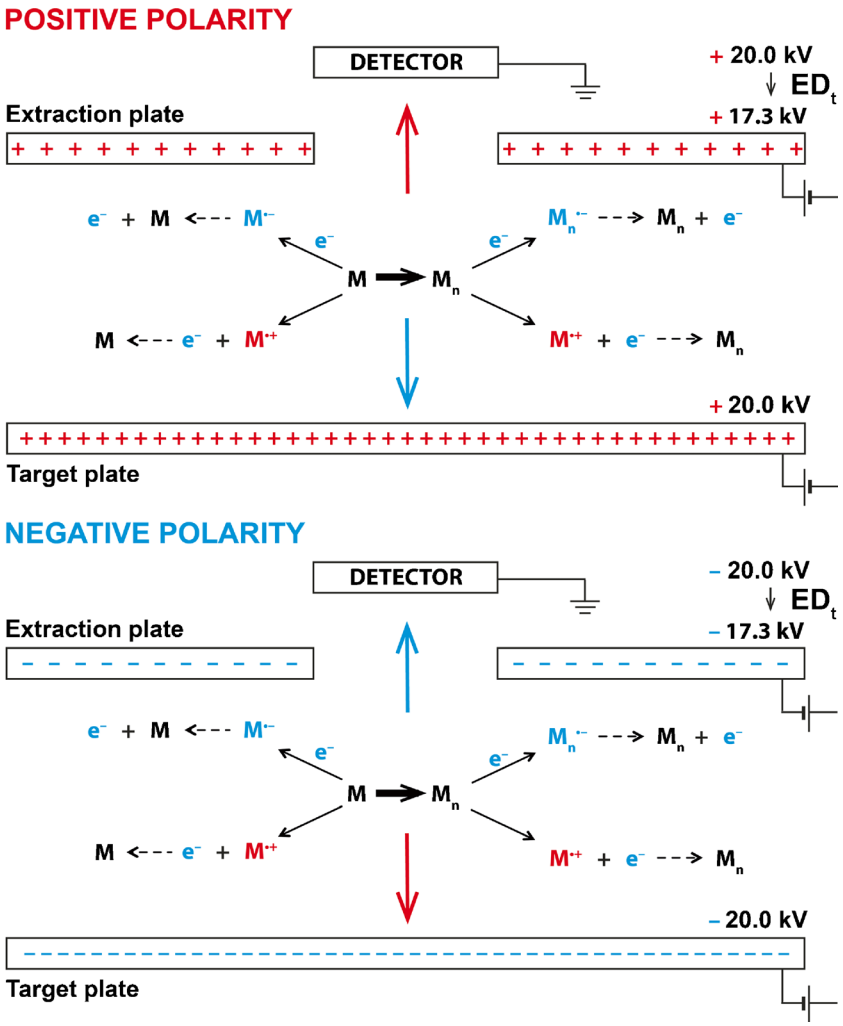

Figure 4. Schematic overview of the proposed mechanisms for positive (top) and negative (bottom) polarity, where ED_t denotes extraction delay time, M fullerene-C_{60}, and M_n fullerene-C_{60} clusters. The thick central arrow indicates the formation of coalesced products. Both M and M_n can react similarly: either electron detachment or attachment occurs, possibly followed by neutralization. Neutralization reactions involving two oppositely charged fullerene-C_{60} entities are not shown. All reactions could occur in principle, but species formation, ion directionality, and detection depend on the polarity, extraction delay time and potential, laser fluence, and the intrinsic unimolecular and bimolecular reactions. Small solid arrows indicate ionization reactions, whereas dashed arrows indicate neutralization reactions

are formed depends on the applied extraction potential and the target plate material's resistivity, since together they determine whether there is enough time for electron attachment to occur. These factors also determine the rate of cation neutralization. Unless cations are neutralized, they have been shown to be stable for the time interval investigated here. Anion neutralization, through EAD, will depend on the plume temperature. Since cluster anions were not observed, no conclusions can be drawn regarding their neutralization but, once formed, they are expected to be more stable than the precursor and fragment anions [43, 44]. We interpret signal intensity differences between polarities to be due to the unimolecular and bimolecular processes that underlie ion formation and neutralization, and the way their reaction rates are influenced by a transient reduction of the extraction potential determined by the substrate material's electrical resistivity.

Since no protons are involved in our experimental design, the number of possible primary ionization pathways is limited. Together with the observed difference between the positive and negative cluster ion signal intensities, (multi-) photon ionization, (photo-) thermal ionization, and energy pooling could still apply. These mechanisms would also support the observed difference between the precursor and fragment ions for opposite polarities. While the work function varies depending on the crystal lattice, temperature, and phase, the role of substrate photoelectron production and subsequent attachment to fullerene-C_{60} is difficult to establish under LDI conditions. Describing the steady and almost linear anion signal intensity increase with increasing target plate material resistivity (at room temperature) in terms of the transient electric field

reduction, a more linear relationship is expected than when a trend had resulted from the lowering of the substrate material's work function, which in turn would be expected to affect the anion signal intensity due to the attachment of additionally produced photoelectrons to fullerene-C_{60}. The presence of additional photoelectrons from the target plate would, based on the high electron attachment cross sections reported for fullerene-C_{60}, have resulted in an overall higher anion yield. Hence, the role of photoelectrons is deemed to be of less importance than that of the substrate material's resistivity.

Conclusions and Outlook

Our results clearly show that the substrate material has an important effect on the ion signal intensity, and care should be taken when comparing results generated with different substrate materials. Electrical resistivity has a clear influence on the precursor and fragment anion signal intensity and possibly on the precursor and fragment cation signal intensity, although this is obscured by formation of cluster cations and delayed ionization. In general, the precursor and fragment cation and anion signal intensity difference becomes smaller upon using a target plate material with a higher resistivity.

Cluster anions are hardly, if at all, formed, which could be due to the chosen extraction potential settings and should be investigated in more depth by varying this parameter systematically. Cluster cations, however, are predominantly formed at intermediate laser fluence (ca. 1.96 Jcm^{-2}), but at higher laser fluences precursor and fragment cations are more readily formed.

Highly electrically resistive target plate materials promote anion formation, most notably Inconel 625 and Ti90/Al6/V4, for which the anion signal intensity exceeded the cation signal intensity by a factor of ~1.4. We interpret this to be due to a transient electric field reduction (the extent of local field reduction depending on the substrate material's resistivity and, therefore, its capability to recharge the surface after cation neutralization), making electron extraction from the plume less effective and allowing more electron attachment (and possibly neutralization) reactions to occur. In order to verify our results, a dual-TOF setup could prove beneficial. However, the target plate should be grounded and the detectors should have equal but oppositely charged potential differences [59, 60]. Finally, working with fullerene-C_{60} has the advantage that proton transfer reactions are absent. Of course, proton transfer is an important aspect of the initial charge separation step and this should, therefore, be investigated in detail with commonly used MALDI matrices.

Acknowledgments

This research was financially supported by the Research Executive Agency (REA) of the European Union under Grant Agreement number PITN-GA-2010-264772 (ITN CHEBANA) and by ETH internal funding under project number ETH-22 11-2. The authors thank Professor Andrea Sinz, Institute of Pharmacy, Martin Luther University, Halle-Wittenberg, Germany, for allowing the initial measurements to be performed on the Ultraflex III, as well as for her advice. Special thanks are extended to Professor Dr. Martin Hersberger, Division of Clinical Chemistry and Biochemistry, University Children's Hospital, Zurich, for donating the Autoflex mass spectrometer to our research group. The authors are much indebted to Mr. Christian Marro for his technical support with the deposition setup and the target plate manufacturing, to Mr. Tobias Morf for his assistance with the substrate surface profiling, and to Mr. Robert F. Steinhoff for structuring the data processing and for the meaningful discussions.

References

1. Karas, M., Bachmann, D., Hillenkamp, F.: Influence of the wavelength in high-irradiance ultraviolet-laser desorption mass-spectrometry of organic-molecules. Anal. Chem. **57**, 2935–2939 (1985)
2. Karas, M., Bachmann, D., Bahr, U., Hillenkamp, F.: Matrix-assisted ultraviolet-laser desorption of nonvolatile compounds. Int. J. Mass Spectrom. Ion Process. **78**, 53–68 (1987)
3. Knochenmuss, R., Zenobi, R.: MALDI ionization: the role of in-plume processes. Chem. Rev. **103**, 441–452 (2003)
4. Zenobi, R., Knochenmuss, R.: Ion formation in MALDI mass spectrometry. Mass Spectrom. Rev. **17**, 337–366 (1998)
5. Ehring, H., Karas, M., Hillenkamp, F.: Role of photoionization and photochemistry in ionization processes of organic-molecules and relevance for matrix-assisted laser desorption ionization mass-spectrometry. Org. Mass Spectrom. **27**, 472–480 (1992)
6. Kovalenko, L.J., Maechling, C.R., Clemett, S.J., Philippoz, J.M., Zare, R.N., Alexander, C.M.O.: Microscopic organic-analysis using 2-step laser mass-spectrometry - application to meteoritic acid residues. Anal. Chem. **64**, 682–690 (1992)
7. Allwood, D.A., Dyer, P.E., Dreyfus, R.W.: Ionization modelling of matrix molecules in ultraviolet matrix-assisted laser desorption/ionization. Rapid Commun. Mass Spectrom. **11**, 499–503 (1997)
8. Allwood, D.A., Dyer, P.E., Dreyfus, R.W., Perera, I.K.: Plasma modelling of matrix assisted UV laser desorption ionisation (MALDI). Appl. Surf. Sci. **109**, 616–620 (1997)
9. Knochenmuss, R., Zhigilei, L.V.: Molecular dynamics model of ultraviolet matrix-assisted laser desorption/ionization including ionization processes. J. Phys. Chem. B **109**, 22947–22957 (2005)
10. Knochenmuss, R.: A quantitative model of ultraviolet matrix-assisted laser desorption/ionization. J. Mass Spectrom. **37**, 867–877 (2002)
11. Liu, B.H., Charkin, O.P., Klemenko, N., Chen, C.W., Wang, Y.S.: Initial ionization reaction in matrix-assisted laser desorption/ionization. J. Phys. Chem. B **114**, 10853–10859 (2010)
12. Chang, W.C., Huang, L.C.L., Wang, Y.S., Peng, W.P., Chang, H.C., Hsu, N.Y., Yang, W.B., Chen, C.H.: Matrix-assisted laser desorption/ionization (MALDI) mechanism revisited. Anal. Chim. Acta **582**, 1–9 (2007)
13. Knochenmuss, R., Karbach, V., Wiesli, U., Breuker, K., Zenobi, R.: The matrix suppression effect in matrix-assisted laser desorption/ionization: application to negative ions and further characteristics. Rapid Commun. Mass Spectrom. **12**, 529–534 (1998)
14. Karas, M., Gluckmann, M., Schafer, J.: Ionization in matrix-assisted laser desorption/ionization: singly charged molecular ions are the lucky survivors. J. Mass Spectrom. **35**, 1–12 (2000)
15. Jaskolla, T.W., Karas, M.: Compelling evidence for Lucky Survivor and gas-phase protonation: the unified MALDI analyte protonation mechanism. J. Am. Soc. Mass Spectrom. **22**, 976–988 (2011)
16. Chen, X.J., Carroll, J.A., Beavis, R.C.: Near-ultraviolet-induced matrix-assisted laser desorption/ionization as a function of wavelength. J. Am. Soc. Mass Spectrom. **9**, 885–891 (1998)
17. Dashtiev, M., Wafler, E., Rohling, U., Gorshkov, M., Hillenkamp, F., Zenobi, R.: Positive and negative analyte ion yield in matrix-assisted laser desorption/ionization. Int. J. Mass Spectrom. **268**, 122–130 (2007)
18. Knochenmuss, R.: Photoionization pathways and free electrons in UV-MALDI. Anal. Chem. **76**, 3179–3184 (2004)

19. Brown, R.S., Lennon, J.J.: Mass resolution improvement by incorporation of pulsed ion extraction in a matrix-assisted laser-desorption ionization linear time-of-flight mass-spectrometer. Anal. Chem. **67**, 1998–2003 (1995)
20. Wiley, W.C., Mclaren, I.H.: Time-of-flight mass spectrometer with improved resolution. Rev. Sci. Instrum. **26**, 1150–1157 (1955)
21. Guenther, S., Koestler, M., Schulz, O., Spengler, B.: Laser spot size and laser power dependence of ion formation in high resolution MALDI imaging. Int. J. Mass Spectrom. **294**, 7–15 (2010)
22. Lai, Y.H., Chen, B.G., Lee, Y.T., Wang, Y.S., Lin, S.H.: Contribution of thermal energy to initial ion production in matrix-assisted laser desorption/ionization observed with 2,4,6-trihydroxyacetophenone. Rapid Commun. Mass Spectrom. **28**, 1716–1722 (2014)
23. Smalley, R.E.: Self-assembly of the fullerenes. Acc. Chem. Res. **25**, 98–105 (1992)
24. Takahata, Y., Hara, T., Narita, S., Shibuya, T.: Ionization energies, electron affinities, and absorption spectrum of fullerene C-60 calculated with the semiempirical HAM/3 and CNDO/S methods. Theochem. J. Mol. Struct. **431**, 219–227 (1998)
25. de Vries, J., Steger, H., Kamke, B., Menzel, C., Weisser, B., Kamke, W., Hertel, I.V.: Single-photon ionization of C-60-fullerene and C-70-fullerene with synchrotron radiation – determination of the ionization-potential of C-60. Chem. Phys. Lett. **188**, 159–162 (1992)
26. Gao, C.Z., Wopperer, P., Dinh, P.M., Suraud, E., Reinhard, P.G.: On the dynamics of photo-electrons in C-60. J. Phys. B At. Mol. Opt. **48**, 105102 (2015)
27. Zimmerman, J.A., Eyler, J.R., Bach, S.B.H., Mcelvany, S.W.: Magic number carbon clusters—ionization potentials and selective reactivity. J. Chem. Phys. **94**, 3556–3562 (1991)
28. Yoo, R.K., Ruscic, B., Berkowitz, J.: Vacuum ultraviolet photoionization mass-spectrometric study of C-60. J. Chem. Phys. **96**, 911–918 (1992)
29. Reynolds, P.J.: North-Holland: Amsterdam, New York (1993)
30. Wang, L.S., Conceicao, J., Jin, C.M., Smalley, R.E.: Threshold photodetachment of Cold C60-. Chem. Phys. Lett. **182**, 5–11 (1991)
31. Yang, S.H., Pettiette, C.L., Conceicao, J., Cheshnovsky, O., Smalley, R.E.: Ups of buckminsterfullerene and other large clusters of carbon. Chem. Phys. Lett. **139**, 233–238 (1987)
32. Lykke, K.R., Wurz, P.: Direct Detection of neutral products from photodissociated-C60. J. Phys. Chem. US **96**, 3191–3193 (1992)
33. Jaffke, T., Illenberger, E., Lezius, M., Matejcik, S., Smith, D., Mark, T.D.: Formation of C60(-) and C70(-) by free-electron capture—activation-energy and effect of the internal energy on lifetime. Chem. Phys. Lett. **226**, 213–218 (1994)
34. Garden, R.W., Sweedler, J.V.: Heterogeneity within MALDI samples as revealed by mass spectrometric imaging. Anal. Chem. **72**, 30–36 (2000)
35. Taylor, R., Parsons, J.P., Avent, A.G., Rannard, S.P., Dennis, T.J., Hare, J.P., Kroto, H.W., Walton, D.R.M.: Degradation of C60 by light. Nature **351**, 277 (1991)
36. Hare, J.P., Kroto, H.W., Taylor, R.: Preparation and UV visible spectra of fullerenes C60 and C70. Chem. Phys. Lett. **177**, 394–398 (1991)
37. Barrow, M.P., Drewello, T.: Significant interferences in the post source decay spectra of ion-gated fullerene and coalesced carbon cluster ions. Int. J. Mass Spectrom. **203**, 111–125 (2000)
38. Atamny, F., Baiker, A., Muhr, H.J., Nesper, R.: Afm and Xrd investigation of crystalline vapor-deposited C-60 films. Fresenius J. Anal. Chem. **353**, 433–438 (1995)
39. Senthilkumar, V., Vickraman, P., Jayachandran, M., Sanjeeviraja, C.: Structural and optical properties of indium tin oxide (ITO) thin films with different compositions prepared by electron beam evaporation. Vacuum **84**, 864–869 (2010)
40. Beer, A.C., Willardson, R.K.: Physics of III-V compounds. In: Semiconductors and semimetals, vol 2. Academic Press, New York (1966)
41. Yeretzian, C., Hansen, K., Diederich, F., Whetten, R.L.: Coalescence reactions of fullerenes. Nature **359**, 44–47 (1992)
42. Prabhudesai, V.S., Nandi, D., Krishnakumar, E.: Low energy electron attachment to C-60. Eur. Phys. J. D. **35**, 261–266 (2005)
43. Ptasinska, S., Echt, O., Denifl, S., Stano, M., Sulzer, P., Zappa, F., Stamatovic, A., Scheier, P., Märk, T.D.: Electron attachment to higher fullerenes and to Sc3N@C-80. J. Phys. Chem. A **110**, 8451–8456 (2006)
44. Elhamidi, O., Pommier, J., Abouaf, R.: Low energy electron impact on C-76 and C-84: excitation, metastable anion formation, and lifetime. Int. J. Mass Spectrom. **205**, 17–25 (2001)
45. Wurz, P., Lykke, K.R.: Kinetics of multiphoton excitation and fragmentation of C-60. Chem. Phys. **184**, 335–346 (1994)
46. Berkowitz, J.: Sum rules and the photoabsorption cross sections of C-60. J. Chem. Phys. **111**, 1446–1453 (1999)
47. Reinkoster, A., Korica, S., Prumper, G., Viefhaus, J., Godehusen, K., Schwarzkopf, O., Mast, M., Becker, U.: The photoionization and fragmentation of C-60 in the energy range 26–130 eV. J. Phys. B Atomic Mol. Opt. **37**, 2135–2144 (2004)
48. Vostrikov, A.A., Dubnov, D.Y., Agarkov, A.A.: Inelastic interaction of an electron with a C-60 cluster. High Temp. **39**, 22–30 (2001)
49. Kasperovich, V., Tikhonov, G., Kresin, V.V.: Low-energy electron capture by free C-60 and the importance of polarization interaction. Chem. Phys. Lett. **337**, 55–60 (2001)
50. Huang, J., Carman, H.S., Compton, R.N.: Low-energy-electron attachment to C-60. J. Phys. Chem. US **99**, 1719–1726 (1995)
51. Vasilev, Y.V., Tuktarov, R.F., Mazunov, V.A.: Resonant electron capture mass spectra of fullerenes C-60 and C-70. Rapid Commun. Mass Spectrom. **11**, 757–761 (1997)
52. Klaiman, S., Gromov, E.V., Cederbaum, L.S.: All for one and one for all: accommodating an extra electron in C-60. Phys. Chem. Chem. Phys. **16**, 13287–13293 (2014)
53. Vasil'ev, Y.V., Abzalimov, R.R., Nasibullaev, S.K., Drewello, T.: C-60(-) mean lifetime as a function of electron energy and molecular temperature. Fuller. Nanotube Carbon Nanostruct. **12**, 229–234 (2004)
54. Liu, Z.Y., Wang, C.R., Huang, R.B., Zheng, L.S.: Mass-distribution of C-60 and C-70 coalescence products produced by direct laser vaporization. Int. J. Mass Spectrom. Ion Process. **145**, 1–7 (1995)
55. Momma, C., Chichkov, B.N., Nolte, S., von Alvensleben, F., Tunnermann, A., Welling, H., Wellegehausen, B.: Short-pulse laser ablation of solid targets. Opt. Commun. **129**, 134–142 (1996)
56. Menzel, C., Dreisewerd, K., Berkenkamp, S., Hillenkamp, F.: The role of the laser pulse duration in infrared matrix-assisted laser desorption/ionization mass spectrometry. J. Am. Soc. Mass Spectrom. **13**, 975–984 (2002)
57. Dreisewerd, K., Schurenberg, M., Karas, M., Hillenkamp, F.: Matrix-assisted laser desorption/ionization with nitrogen lasers of different pulse widths. Int. J. Mass Spectrom. Ion Process. **154**, 171–178 (1996)
58. Kobayashi, T., Matsuo, Y.: Study on the carbon fragment anions produced by femtosecond laser ablation of solid C-60. J. Chem. Phys. **134**, 064320 (2011)
59. Tsai, S.T., Chen, C.W., Huang, L.C.L., Huang, M.C., Chen, C.H., Wang, Y.S.: Simultaneous mass analysis of positive and negative ions using a dual-polarity time-of-flight mass spectrometer. Anal. Chem. **78**, 7729–7734 (2006)
60. Lai, Y.H., Wang, C.C., Lin, S.H., Lee, Y.T., Wang, Y.S.: Solid-phase thermodynamic interpretation of ion desorption in matrix-assisted laser desorption/ionization. J. Phys. Chem. B **114**, 13847–13852 (2010)